*Journal of Applied Mechanics and Technical Physics, Vol. 41, No. 4, 2000*

# EXPERIMENTAL AND NUMERICAL MODELING OF THE TURBULENT WAKE OF A SELF-PROPELLED BODY

**N. V. Gavrilov, A. G. Demenkov,[1] V. A. Kostomakha, and G. G. Chernykh[1]**

UDC 532.517.4

*The development of the turbulent axisymmetric wake of a self-propelled body is modeled experimentally and numerically. Experimentally, the self-propulsion regime was implemented in the wake of a body of revolution whose hydrodynamic resistance was completely compensated by the pulse of a swirling jet rejected from its trailing part, and the jet-induced swirling was counterbalanced by the rotation of a part of the body surface in the opposite direction. The second-order semiempirical turbulence model that includes the differential equation of motion, the transfer of the normal Reynolds stresses, and the dissipation rate was used to describe this wake mathematically, and the nonequilibrium algebraic relations were used to determine the tangential stresses. A satisfactory agreement between the calculation results and the experimental data is shown. Degeneration of the distant turbulent wake is investigated numerically.*

**1.** The problem of the evolution of the turbulent wake of a body of revolution that moves uniformly and rectilinearly in an unbounded homogeneous incompressible fluid is considered. The body is equipped with a propeller whose thrust compensates for the drag, so that the longitudinal component of the total redundant momentum $J$ in the wake is zero. Generally, the propulsor can swirl the fluid in the wake; therefore, for the body not to rotate about its longitudinal axis, swirling should be compensated for in one way or another. Here the total moment of momentum $M$ in the wake is equal to zero. This mode of motion is called a mode of self-propulsion.

In all the previous experimental studies in which the wake of a self-propelled body was modeled and studied, nonswirling [1–7] or swirling [8, 9] jets were used as propulsors or the required thrust was generated by a propeller [10–12]. In the absence of swirling, attention was given to satisfaction of the condition $J = 0$, which is sufficient for creation of the mode of self-propulsion. However, in the presence of rotational motion in the wake, the circumferential velocity component not only contributes to the total momentum, but also results in the emergence of the moment of momentum in the wake.

It follows from an analysis of the cited literature that in all the experiments performed with flow-swirling propulsors, appropriate forces were taken up by one structure or another that supports the model (for example, tension members for wind-tunnel experiments), and the quantity $M$ calculated for the wake of such a model is not zero. In this study, this drawback of the experimental self-propulsion modeling is eliminated owing to the construction of a model that makes it possible to change the thrust of a propulsor independently and compensate for the flow swirling created by this propulsor.

The first studies concerning numerical modeling of swirling turbulent wakes are reviewed by Shets [10]. In [10], calculation results obtained with the use of a simplified turbulence $\varepsilon$-model are presented and

Lavrent'ev Institute of Hydrodynamics, Siberian Division, Russian Academy of Sciences, Novosibirsk 630090. [1]Institute of Computing Technologies, Siberian Division, Russian Academy of Sciences, Novosibirsk 630090. Translated from Prikladnaya Mekhanika i Tekhnicheskaya Fizika, Vol. 41, No. 4, pp. 49–58. July–August, 2000. Original article submitted September 24, 1999; revision submitted November 5, 1999.

0021-8944/00/4104-0619 $25.00  

the drawbacks related to the use of the algebraic Reynolds-stress models and the more general second-order differential models, which, probably, are due to incomplete experimental data, are indicated. A calculation–theoretical modeling of swirling wakes was performed in [13–15], in which the self-similarity and degeneration laws for wakes with a different degree of compensation relative to the moment of momentum and the influence of background turbulence on the flow evolution in the wake was studied. The classical ($e$–$\varepsilon$)-model of turbulence was used in these studies. Degeneration of the Reynolds stresses was not analyzed. The strong sensitivity of the defect of the longitudinal velocity component to the initial unbalance of the momentum and the weak dependence of the circumferential velocity component, the turbulence energy, and the wake width on it were shown. An analysis of the asymptotic behavior of average-velocity perturbations has allowed one to establish that the presence of even a small tangential velocity component noticeably influences the flow pattern.

The swirling momentumless turbulent wake with the nonzero moment of momentum that is based on the hierarchy of second-order semiempirical turbulence models is modeled numerically in [16, 17]. It is shown that a satisfactory agreement with experimental data [9] can be obtained with the use of a mathematical model that includes the differential transfer equations of the normal Reynolds stresses and one tangential Reynolds stress and nonequilibrium algebraic relations for other tangential stresses.

Based on an analysis of the results of calculation-theoretical modeling of swirling turbulent wakes, one can conclude that there are no satisfactory numerical models of the swirling turbulent wakes of self-propellant bodies. The present work was performed with a view toward bridging the gaps available in the study of this problem.

**2.** To describe the flow, we use the following system of averaged equations of motion, continuity, and transfer of normal Reynolds stresses $\langle u'^2\rangle$, $\langle v'^2\rangle$, and $\langle w'^2\rangle$ in the approximation of a thin shear layer:

$$U\frac{\partial U}{\partial x}+V\frac{\partial U}{\partial r}=-\frac{1}{r}\frac{\partial}{\partial r}r\langle u'v'\rangle+\frac{\partial}{\partial x}\int_r^\infty\frac{W'^2+\langle w'^2\rangle-\langle v'^2\rangle}{r}\,dr-\frac{\partial(\langle u'^2\rangle-\langle v'^2\rangle)}{\partial x}; \tag{1}$$

$$U\frac{\partial W}{\partial x}+V\frac{\partial W}{\partial r}+\frac{VW}{r}=-\frac{1}{r}\frac{\partial}{\partial r}r\langle v'w'\rangle-\frac{\langle v'w'\rangle}{r}-\frac{\partial\langle u'w'\rangle}{\partial x}; \tag{2}$$

$$\frac{\partial U}{\partial x}+\frac{\partial V}{\partial r}+\frac{V}{r}=0; \tag{3}$$

$$U\frac{\partial\langle u'^2\rangle}{\partial x}+V\frac{\partial\langle u'^2\rangle}{\partial r}=-2(1-\alpha)\langle u'v'\rangle\frac{\partial U}{\partial r}-\frac{2}{3}\varepsilon-C_1\frac{\varepsilon}{e}\Big(\langle u'^2\rangle-\frac{2}{3}e\Big)$$
$$+\frac{2}{3}\alpha P+\frac{C_s}{r}\frac{\partial}{\partial r}\Big(\frac{re\langle v'^2\rangle}{\varepsilon}\frac{\partial\langle u'^2\rangle}{\partial r}\Big); \tag{4}$$

$$U\frac{\partial\langle v'^2\rangle}{\partial x}+V\frac{\partial\langle v'^2\rangle}{\partial r}-2\frac{W}{r}\langle v'w'\rangle=2(1-\alpha)\langle v'w'\rangle\frac{W}{r}-\frac{2}{3}\varepsilon$$
$$-C_1\frac{\varepsilon}{e}\Big(\langle v'^2\rangle-\frac{2}{3}e\Big)+\frac{C_s}{r}\frac{\partial}{\partial r}\Big[\frac{re}{\varepsilon}\Big(\langle v'^2\rangle\frac{\partial\langle v'^2\rangle}{\partial r}-\frac{2\langle v'w'\rangle^2}{r}\Big)\Big]$$
$$-\frac{2C_se}{r\varepsilon}\Big(\langle v'w'\rangle\frac{\partial\langle v'w'\rangle}{\partial r}+\langle w'^2\rangle\frac{\langle v'^2\rangle-\langle w'^2\rangle}{r}\Big)+\frac{2}{3}\alpha P; \tag{5}$$

$$U\frac{\partial\langle w'^2\rangle}{\partial x}+V\frac{\partial\langle w'^2\rangle}{\partial r}+2\frac{W}{r}\langle v'w'\rangle=-2(1-\alpha)\langle v'w'\rangle\frac{\partial W}{\partial r}-\frac{2}{3}\varepsilon$$
$$-C_1\frac{\varepsilon}{e}\Big(\langle w'^2\rangle-\frac{2}{3}e\Big)+\frac{C_s}{r}\frac{\partial}{\partial r}\Big[\frac{re}{\varepsilon}\Big(\langle v'^2\rangle\frac{\partial\langle w'^2\rangle}{\partial r}+\frac{2\langle v'w'\rangle^2}{r}\Big)\Big]$$

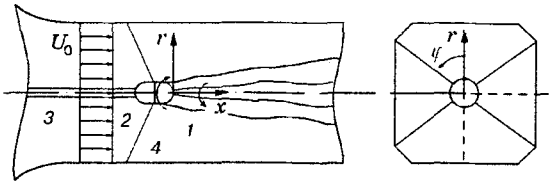


Fig. 1

$$+\frac{2C_s e}{r\varepsilon}\Big(\langle v'w'\rangle\frac{\partial\langle v'w'\rangle}{\partial r}+\langle w'^2\rangle\frac{\langle v'^2\rangle-\langle w'^2\rangle}{r}\Big)+\frac{2}{3}\alpha P. \tag{6}$$

Here $(x, r, \varphi)$ is the cylindrical coordinate system with the origin at the trailing edge of the body (Fig. 1), the $x$ axis is directed in the direction opposite to the body motion, $U$, $V$, $W$, $u'$, $v'$, and $w'$ are the corresponding velocity components of the averaged and pulsatory motions, $\langle u'v'\rangle$, $\langle u'w'\rangle$, and $\langle v'w'\rangle$ are the tangential Reynolds stresses, and $e = (\langle u'^2\rangle + \langle v'^2\rangle + \langle w'^2\rangle)/2$ is the turbulence energy. The angle brackets mean averaging. The terms with molecular viscosity are discarded in the smallness assumption.

The tangential turbulent stresses are determined from the Rodi nonequilibrium algebraic relations [18]

$$\langle u'v'\rangle = \alpha_1\langle v'^2\rangle\frac{\partial U}{\partial r}, \tag{7}$$

$$\langle u'w'\rangle = \alpha_1\Big(\langle u'v'\rangle\frac{\partial W}{\partial r}+\langle v'w'\rangle\frac{\partial U}{\partial r}\Big), \tag{8}$$

$$\langle v'w'\rangle = \alpha_1\Big(\langle v'^2\rangle r\frac{\partial(W/r)}{\partial r}+\frac{W}{r}(\langle v'^2\rangle-\langle w'^2\rangle)\Big), \tag{9}$$

where $\alpha_1 = -\lambda_1 e/\varepsilon$ and $\lambda_1 = (1 - C_2)/(C_1 + P/\varepsilon - 1)$.

The dissipation rate $\varepsilon$ was found by solving the differential transfer equation

$$U\frac{\partial\varepsilon}{\partial x}+V\frac{\partial\varepsilon}{\partial r}=\frac{C_\varepsilon}{r}\frac{\partial}{\partial r}\Big(\frac{re\langle v'^2\rangle}{\varepsilon}\frac{\partial\varepsilon}{\partial r}\Big)+\frac{\varepsilon}{e}(C_{\varepsilon 1}P-C_{\varepsilon 2}\varepsilon). \tag{10}$$

In Eqs. (4)-(6) and (10) and relations (7)-(9), the amount of turbulence energy produced owing to the averaged motion has the form

$$P = -\Big(\langle u'v'\rangle\frac{\partial U}{\partial r}+\langle v'w'\rangle r\frac{\partial(W/r)}{\partial r}\Big).$$

In formulas (1)-(10), the empirical constants are as follows: $C_s = 0.22$, $C_\varepsilon = 0.17$, $\alpha = 0.93$, $C_1 = 0.6$, $C_2 = 2.2$, $C_{\varepsilon 1} = 1.45$, and $C_{\varepsilon 2} = 1.92$. The variables of the problem were dimensionalized by using the undisturbed-flow velocity $U_0$ and the characteristic length $D$ (diameter of the body) as the scales. The mathematical model given above is based on the model from [19]. The structure of the mathematical model is due to the experience in numerical modeling of nonswirling momentumless turbulent wakes in a linearly stratified fluid [20]. The calculations of the present study represent the initial stage of the problem of numerical modeling of the swirling turbulent wakes of self-propellant bodies in a stratified fluid.

As the initial conditions for $x = x_0$, we set the transverse distributions $U$, $W$, $\varepsilon$, and $\langle u_i'u_i'\rangle$ ($i = 1, 2$, and 3) consistent with experimental data. The undisturbed-flow conditions were specified as $r \to \infty$ and the symmetry conditions for $U$, $\langle u_i'u_i'\rangle$, and $\varepsilon$ for $r = 0$ and the antisymmetry conditions for $V$ and $W$:

$$\frac{\partial U}{\partial r}=\frac{\partial\langle u_i'u_i'\rangle}{\partial r}=\frac{\partial\varepsilon}{\partial r}=V=W=0.$$

The conservation laws for the total redundant momenta and the moment of momentum follow from the mathematical model and appropriate initial and boundary conditions:

$$J(x) = 2\pi\rho_0\int_0^\infty r\Big(UU_1+\langle u'^2\rangle-\frac{W^2+\langle v'^2\rangle+\langle w'^2\rangle}{2}\Big)\,dr = J(x_0); \tag{11}$$

$$M(x) = 2\pi\rho_0 \int_0^\infty (UW + \langle u'w' \rangle) r^2 \, dr = M(x_0). \tag{12}$$

Here $U_1 = U - U_0$ is the defect of the longitudinal velocity component and $\rho_0 = \text{const}$ is the fluid density.

The numerical realization of the model is based on the use of a first-order, finite-difference algorithm of the approximation on mobile grids that is conservative relative to the conservation laws (11) and (12). The algorithm and its testing are given in detail in [16, 21]; therefore, we only note that in approximating Eq. (2), in the half-integer nodes of the grid, in the variable $r$ the values of the turbulent-viscosity coefficient $\nu_{tw} = \alpha_1 \langle v'^2 \rangle$ were calculated from the formula [22]

$$(\nu_{tw})_{i\pm1/2} = \frac{2(\nu_{tw})_{i\pm1}(\nu_{tw})_i}{(\nu_{tw})_{i\pm1} + (\nu_{tw})_i}.$$

From the difference approximation (2), we obtain a finite difference analog of the conservation law

$$J_1(x) = 2\pi\rho_0 \int_0^\infty \left[ UU_1 - \int_r^\infty \frac{W'^2 + \langle w'^2 \rangle - \langle v'^2 \rangle}{r'} \, dr' + \langle u'^2 \rangle - \langle v'^2 \rangle \right] r \, dr = J_1(x_0)$$

equivalent to (11). Here it is assumed that all appropriate mathematical procedures are correct.

**3.** The experiments were carried out in a low-turbulence wind tunnel whose length is 4 m and whose characteristic transverse cross section is $0.4 \times 0.4$ m. The disposition of the model is shown schematically in Fig. 1. The model is made from an aluminum alloy and is a body of revolution composed from half of an ellipsoid of revolution with 25- and 35-mm semiaxes in the leading part, a circular cylinder of length 40 mm in the central part, and the second half of the ellipsoid in the trailing part. The total length of the model is 110 mm, and its diameter is $D = 50$ mm.

The model consists of mobile and fixed parts (Fig. 1, 1 and 2, respectively). In the fixed part of the model, which is supported by the compressed air-supply tube 3 and the tension members 4, an injector and a DC micromotor are built in. The diameter of the output orifice of the injector is 6 mm. The mobile part of the model is put into rotation by the micromotor through an internal frictional hook. The model is positioned on the axis of symmetry of the working part 5 of the tube at zero angle of attack to the incoming flow. The mode of operation of the injector and the rotational velocity of the model surface were chosen by varying the air flow rate through the injector and the power-supply voltage of the micromotor. The self-propulsion condition ($J = 0$ and $M = 0$) was assumed to be satisfied if the ratio of the positive part of the integrand in (11) and (12) to the negative part was $1.00 \pm 0.05$. The experiments were performed for an air velocity of $U_0 = 15$ m/sec in the working part of the wind tunnel, which corresponds to the Reynolds number $\mathrm{Re} = U_0 D/\nu = 5 \cdot 10^4$ ($\nu$ is the kinematic-viscosity coefficient).

The measurements were carried out by a thermoanemometer equipped with a linearizer. We used single- and double-filament gauges made from gold-plated tungsten of diameter 5 $\mu$m and length 1.25 mm. According to the measurement technique of [9], the gauges at each measuring point were oriented relative to the mean-velocity vector. The experimental data were computer-processed.

**4.** In the experiments, the transverse distributions of three components of the average-velocity vector and the normal and tangential Reynolds stresses in the cross sections of the wake $x/D = 5$, 7.5, 10, 20, 30, and 46 were measured. The profile of the turbulence-energy dissipation rate $\varepsilon$ was found only for $x/D = 10$. At the same time, before the main series of experiments, in which the quantities $J$ and $M$ were assumed to be zero, the profiles $U_1$ and $\langle u'^2 \rangle^{1/2}$ were measured under the conditions where the mobile part of the model did not rotate and the jet in the trailing part was not blown out. These data were used at the stage of installation of the model at zero angle of attack and to calculate the drag coefficient of the body $c_x = 8F_x/(\pi\rho_0 D^2 U_0^2)$, where the force of hydrodynamic resistance was calculated from the formula $F_x = 2\pi\rho_0 \int_0^\infty U_0 U_1 r \, dr$. We obtained $c_x = 0.2$, which indicates that the model is well streamlined.

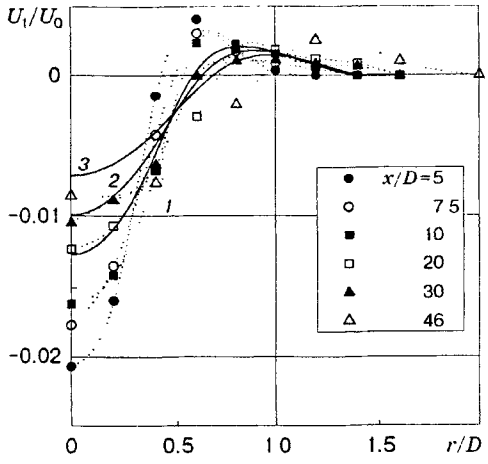


Fig. 2

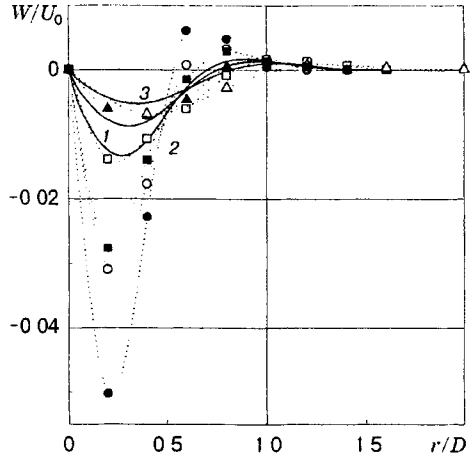


Fig. 3

In the mode of self-propulsion, the distributions $U_1(r,x)$ always have the characteristic feature, i.e., the regions in which $U_1 < 0$ and $U_1 > 0$. The negative values of $U_1$, which are observed on the profiles in Fig. 2, are caused by the fluid decelerated in the boundary layer on the body, whereas the positive values $U_1$ are ensured by a jet propulsor. Solid curves 1-3 in Fig. 2 show calculation results for $x/D = 20$, 30, and 46. The initial data were set for $x/D = 10$.

In the calculations, the boundary conditions for $U_1$, $W$, $e$, $\varepsilon$, and $\langle u_i'^2 \rangle$ were transferred from infinity on the line $r = r_* = 4D$ ($r_*$ was determined in numerical experiments). The main calculation results were obtained on an $r$-uniform grid with step $h_r/D = 0.02$. The grid step $h_x/D$ on the longitudinal coordinate increased and changed from 0.01 by the formula of the member of a geometrical progression with a denominator equal to 1.006. To monitor the accuracy, a calculation for $h_r/D = 0.04$ and the initial value of $h_x/D = 0.02$ was carried out. The deviations of the grid solutions in a norm that is a grid analog of the norm of continuous-function space did not exceed 1%.

One can see that the numerical model constructed describes quite exactly the behavior of $U_1(r,x)$ in the preaxial wake zone and with smaller accuracy at the periphery. The latter is connected with the drawback inherent in the second-order mathematical models of turbulence, which do not incorporate flow intermittency in the outer regions of the wake.

The same injector as in the experiment with a sphere [9] was used as a device which swirls the flow and creates a jet that compensates for the body drag. The rotation in the jet was counterclockwise. To attain the zero total moment of momentum, a part of the body surface rotated in the opposite direction. The measured distributions of the circumferential component of the average-velocity vector $W(r,x)$ depicted in Fig. 3 show that the fluid rotates in one direction in the near-axial region of the wake and in the other direction in the peripheral annular region of the wake. The presence of this additional rotary motion also determines the basic differences of the realized mode of self-propulsion from those studied previously. For small $r$, the relation $W(r,x) \approx r$ is fulfilled, i.e., the fluid rotates as a solid.

The maximum value of the circumferential velocity component is of the same order as the value of the defect of the longitudinal velocity component and is much smaller than the velocity of the incoming flow, which corresponds to the case of weak swirling. Nevertheless, the contribution of the rotational motion in the wake to $J$ was taken into account, and it amounted to 8% for $x/D = 5$ and 2% of the positive part of the first terms in the integrand in (11) for $x/D = 10$.

As one can see in Fig. 3, the calculated profiles $W(r,x)$ are in agreement with the experimental data throughout the wake region. The notations in Figs. 3 and 4 are the same as in Fig. 2.

The radial component of the average-velocity vector is negligible, as in the experiments with a sphere [9].

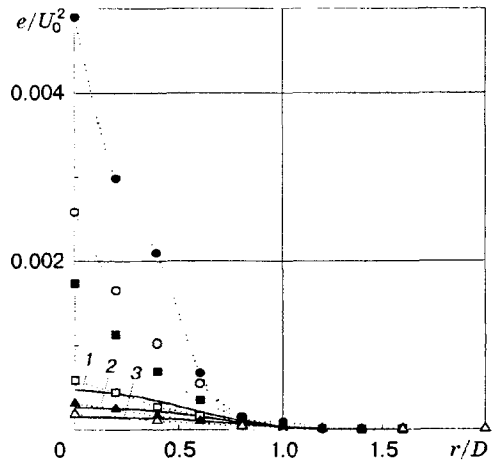


Fig. 4

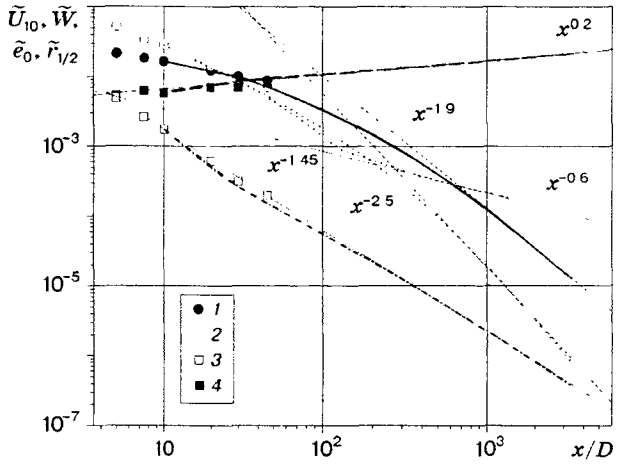


Fig. 5

In momentumless swirling-free wakes, the main body of kinetic energy is concentrated in turbulent fluctuations already at small distances from the body [23]. A similar situation occurs in this case as well (a swirling wake). In particular, the ratio of the total kinetic energy of the pulsatory motion $\int_0^\infty er\,dr$ to the total kinetic energy of the average motion $\int_0^\infty (U_1^2/2+W^2/2)r\,dr$ is 4.9 for a wake cross section of $x/D = 5$ and 6.6 for $x/D = 30$. With increase in $x$, this ratio grows and is 49.2 for $x/D = 200$ according to the calculation results. The significant level of turbulence energy at a small distance from the body is supported by the radial gradients of the longitudinal and circumferential velocity components and corresponding tangential stresses. The experimental results show that both components of turbulence-energy generation in the energy-turbulence balance equation are important, the rotational average-velocity component playing a larger role in the vicinity of the body. This is shown by the ratio

$$\int_0^\infty \langle u'v'\rangle \frac{\partial U_1}{\partial r}\, r\,dr \Big/ \int_0^\infty \langle v'w'\rangle \frac{\partial (W/r)}{\partial r}\, r^2\,dr,$$

which is equal to 0.08 for $x/D = 5$; however, already for the wake cross section ($x/D = 30$), the influence of the longitudinal velocity component becomes more noticeable and the ratio is 1.3; for $x/D = 200$, this ratio is 2.3.

In the course of calculations, the ratio of the turbulence-energy generation $P$ owing to the averaged-motion gradients to the dissipation rate $\varepsilon$ versus $x/D$ was analyzed. We obtained $P/\varepsilon < 0.3$ for $x/D \in [10.46]$. It is known that the classical ($e$–$\varepsilon$)-model of turbulence is suitable only for flows characterized by $P/\varepsilon \approx 1$; therefore, here we use a more complicated mathematical model of turbulence.

The operation of the jet propulsor leads to an increased level of turbulence energy in the neighborhood of the wake axis. This is seen in Fig. 4, where the transverse distributions of the pulsatory energy at different distances from the body are shown. In contrast to similar structures behind a towed body, the maximum values of $e$ are reached on the wake axis in this case. The calculation results for $x/D = 20$, 30, and 46 (solid curves 1–3) agree well with the experimental data.

Figure 5 illustrates the change in the calculated and measured characteristic scales of turbulence as a function of distance from the body. Here $\tilde{U}_{10} = |U_{10}|/U_0$ is the axial value of the defect of the longitudinal velocity component (the solid curve), $\tilde{W} = |W|_{\max}/U_0$ is the maximum value of the circumferential velocity component in this cross section of the wake (dotted curves), $\tilde{e}_0 = e_0/U_0^2$ is the turbulence energy on the

wake axis (the dot-and-dashed curve), and $\tilde{r}_{1/2} = (r_{1/2}/D) \cdot 10^{-2}$ is the characteristic scale of the wake width (the dashed curve) determined from the condition $\langle u'^2 \rangle^{1/2}(r_{1/2}, x) = 0.5\langle u'^2 \rangle^{1/2}(0, x)$ [$\langle u'^2 \rangle^{1/2}(0, x)$ is the rms value of the fluctuations of the longitudinal velocity component on the wake axis]; points 1–4 refer to the corresponding experimental data.

For correctness of the large-distance calculation results, it is necessary to ensure the closeness to zero of the initial values of $J$ and $M$. With this in view, the experimental distributions were approximated by cubic splines, and the needed smallness of the values of $J$ and $M$ was then reached by small variations in the resulting functions for large $r$. Two variants of calculations were carried out: $J = 5.5 \cdot 10^{-13}$ and $M = 5.4 \cdot 10^{-11}$ (for $10 \leqslant x/D \leqslant 3315$) in the first variant and $J = 2.2 \cdot 10^{-12}$ and $M = 4.2 \cdot 10^{-4}$ in the second variant (for $10 \leqslant x/D \leqslant 1464$).

The calculations results for both variants agree with the experimental data, almost coinciding for the scale functions $U_{10}(x)$, $e_0(x)$, and $r_{1/2}(x)$ in the entire range of $x/D$ values considered. The main distinction is observed in the behavior of the function $W_{\max}(x)$ for $x/D > 50$.

At large distances from the body, the dependence of all the scale functions on $x$ is a power dependence (solid thin straight lines in Fig. 5); within the framework of the mathematical model used, this is one necessary indication that the self-similarity of the turbulent motion in the wake is reached. We note the following specific features. If in the turbulent wakes behind the towed bodies the self-similarity is generally reached already at small distances downstream and, primarily, for first-order momenta, in the momentumless and "momentless" wake an asymptotic behavior is first observed for the characteristic transverse dimension of the wake and then for turbulence energy, the characteristic scale of the peripheral velocity $W_{\max}$, and for the defect of the longitudinal velocity component $U_{10}$ only for $x/D > 1000$.

For the first variant of calculation, for large $x/D$ the circumferential velocity component decreases as $W_{\max}(x) \sim x^{-2.5}$, i.e., more rapidly than the axial-velocity defect $U_{10}(x) \sim x^{-1.9}$ and, hence, swirling can be ignored at a certain moment.

It is noteworthy that an analysis of the self-similarity of the turbulent wake for $J = M = 0$ is very complicated (see, e.g., [15]). Our elementary numerical analysis of the asymptotic degeneration is based on processing of the numerical results. It is of interest that in the theoretical study of [24] of swirl laminar flows of a self-propelled sphere, the asymptotic representations $U_{10}(x) \sim x^{-2}$ and $W_{\max} \sim x^{-2.5}$ close to those given in Fig. 5 were obtained on the basis of the exact Navier–Stokes equations.

Despite the closeness of the indicated degeneration laws at all the distances studied, the flow in the wake was a developed turbulent flow. This is supported by the value of the turbulent Reynolds number $\mathrm{Re}_\lambda = \sqrt{2e}\lambda/\nu$ calculated according to the Taylor microscale $\lambda = \sqrt{10e\nu/\varepsilon}$. It follows from the calculations that the axial values of $\mathrm{Re}_\lambda \in [37; 80]$ in the range of $x/D \in [10; 2000]$; here we have $\mathrm{Re}_\lambda \sim x^{-0.25}$ for large $x/D$.

In the second variant of calculations, at large distances from the body the self-similar wake with a finite nonzero moment of momentum occurs. For $x/D > 300$, we have $W_{\max} \sim x^{-0.6}$, which agrees with the condition $M = \mathrm{const}$ [see formula (12)] and the resulting value of the parameter in the wake-expansion law $r_{1/2} \sim x^{0.2}$.

Compared with the wake experiments for a towed body, in our experiments performed at the same distance $x/D = 5$, the wake width is 1/3 smaller, which is due to the creation of a jet propulsor of rarefaction on the wake axis and retardation of the separation of boundary layers on the trailing surface of the body. Taking into account this circumstance and the considerably smaller rate of increase in the transverse dimensions of the wake [$r_{1/2}(x) \sim x^{0.33}$ for axisymmetric turbulent wakes of towed bodies], one can conclude that swirling in the momentumless wake plays a significant stabilizing effect.

Another necessary indication of reaching the self-similarity is the affine similarity of the transverse profiles of the dimensionless turbulence characteristics in the wake. An example of realization of this mode of motion in the wake is the self-similar profiles of the defect of the longitudinal and circumferential velocity components and the turbulence energy in Fig. 6 (the dotted curve refers to the calculation for $x/D = 338$,

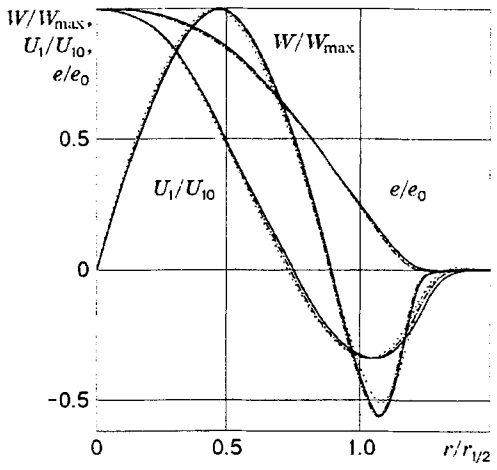


Fig. 6

the dot-and-dashed curve to the calculation for $x/D = 2000$, and the solid curve to the calculation for $x/D = 3315$). As the asymptotic degeneration is reached (see Fig. 5), a similarity of the distributions is observed on the site $x/D > 1000$ in the wake.

Thus, the dynamics of the axisymmetric wake of a self-propelled body has been modeled experimentally. A numerical flow model has been constructed with the use of the second-order semiempirical model of turbulence. The calculation results agree well with the experimental data. A numerical analysis of the degeneration of a distant turbulent wake has been carried out.

This work was partially supported by the Russian Foundation for Fundamental Research (Grant Nos. 95-01-01339 and 98-01-00736).

## REFERENCES

1. E. Naudascher, "Flow in the wake of a self-propelled body and related sources of turbulence," *J. Fluid Mech.*, **22**, No. 4, 625–656 (1965).
2. A. S. Ginevskii, *The Theory of Turbulent Jets and Wakes* [in Russian], Mashinostroenie, Moscow (1969).
3. H. Higuchi and T. Kubota,"Axisymmetric wakes behind a slender body including zero-momentum configurations," *Phys. Fluids*, **A2**, No. 9, 1615–1623 (1990).
4. N. V. Alekseenko and V. A. Kostomakha, "An experimental study of an axisymmetric momentumless turbulent jet flow," *Prikl. Mekh. Tekh. Fiz.*, No. 1, 65–69 (1987).
5. J. M. Cimbala amd M. J. Park, "An investigation of the turbulent structure in a two-dimensional momentumless wake," *J. Fluid Mech.*, **213**, 479–509 (1990).
6. L. N. Ukhanova and M. O. Frankfurt, "An experimental study of two-dimensional momentumless jet flows," *Inzh.-Fiz. Zh.*, **47**, No. 6, 906–911 (1984).
7. Yu. M. Dmitrenko, I. I. Kovalev, N. N. Luchko, and P. Ya. Cherepanov, "A study of a flat turbulent wake with zero redundant momentum," *Inzh.-Fiz. Zh.*, **52**, No.. 5, 743–751 (1987).
8. L. N. Voitovich, "An experimental study of swirling turbulent jet flows," in: *Industrial Aerodynamics. Aerodynamics of Blade Machines. Channels, and Jet Flows* (collected scientific papers) [in Russian], Vol. 1/33, Mashinostoenie, Moscow (1986), pp. 224-238.
9. V. A. Kostomakha and N. V. Lesnova, "Turbulent swirling wake of a sphere with complete or partial compensation of the drag," *Prikl Mekh. Tekh. Fiz.*, **36**, No. 2, 88–98 (1995).
10. J. Shets, *Turbulent Flows. Processes of Injection and Intermixing* [Russian translation], Mir, Moscow (1984).

11. A Sirviente and V. C. Patel, "Experiments in the swirling wake of a self-propelled axisymmetric body," in: *Proc. of the 21st Symp. on Naval Hydrodynamics* (Trondheim, Norway, 24–28 June, 1996). Trondheim (1996), pp. 74–86.
12. T. Faure and G. Robert, "Turbulent kinetic energy balance in the wake of a self-propelled body," *J. Exp. Fluids.*, **21**, No. 4, 268–274 (1996).
13. A. G. Gumilevskii, "A study of momentumless swirling wakes on the basis of the two-parameter model of turbulence," *Izv. Ross. Akad. Nauk. Mekh. Zhidk. Gaza*, No. 3, 35–41 (1992).
14. A. G. Gumilevskii, "Violation of the self-similarity in turbulent axisymmetric wakes with swirling," *Izv. Ross. Akad. Nauk. Mekh. Zhidk. Gaza*, No. 1, 41–47 (1993).
15. A. G. Gumilevskii, "Self-similarity and degeneration laws in wakes with compensation relative to the momentum and the moment of momentum," *Izv. Ross. Akad. Nauk. Mekh. Zhidk. Gaza*, No. 5, 35–41 (1993).
16. G. G. Chernykh, A. G. Demenkov, and V. A. Kostomakha, "Numerical model of a swirling momentumless turbulent wake," *Russ. J. Numer. Anal. Math. Model.*, **13**, No. 4, 279–288 (1998).
17. V. A. Kostomakha, G. G. Chernykh, and A. G. Demenkov, "Experimental and numerical modeling of a swirling turbulent wake," in: *Proc. of the 9th Int. Conf. on Methods of Acrophys. Res.* (Novosibirsk, June 29–July 3, 1998), Part 2, Inst. Theor. Appl. Mech., Sib. Div., Russian Acad. of Sci., Novosibirsk (1998), pp. 112–117.
18. M. A. Sharif and J. K. E. Wong, "Evaluation of the performance of three turbulence closure models in the prediction of confined swirling flows," *Comput. Fluids*, **24**, No. 1, 81–100 (1995).
19. F. Drust, B. E. Launder, F. W. Schmidt, and J. H. Whitelow, in: *Turbulent Shear Flows*, Springer Verlag, Heidelberg–New York (1979).
20. G. G. Chernykh and O. F. Voropayeva, "Numerical modeling of momentumless turbulent wake dynamics in a linearly stratified medium," *Comput. Fluids*, **28**, 281–306 (1999).
21. A. G. Demenkov and G. G. Chernykh, "Numerical modeling of jet flows of a viscous incompressible fluid," *Vychisl. Tekhnol.*, **4**, No. 12, 119–131 (1995).
22. A. N. Tikhonov and A. A. Samarskii, *Equations of Mathematical Physics* [in Russian], Nauka, Moscow (1966).
23. N. N. Fedorova and G. G. Chernyhk, "Numerical modeling of the momentumless turbulent wake of a sphere," *Model. Mekh.*, **6**, No. 1, 129–140 (1992).
24. V. L. Sennitskii, "Motion of inclusions in a vibrating fluid," Doctoral Dissertation in Phys.-Math. Sci., Novosibirsk (1993).